Post-Print

This is the accepted version of:

When citing this work, cite the original published paper.

Dynamical structure of the motion around asteroids with uncertain gravity and solar radiation pressure

Feng J.[1*], Santeramo D.[2], Di Lizia P.[2], Armellin R.[3], Hou X.[4]

[1] University of Strathclyde, UK, jinglang.feng@strath.ac.uk

[2] Politecnico di Milano, Italy   [3] University of Auckland, New Zealand

[4] Nanjing University, China

Abstract

For a rendezvous space mission to a small body, the gravity field is usually modelled with large uncertainty in the preliminary mission design. Consequently, the orbital motion in the vicinity of the body cannot be predicted accurately. In this research, the automatic domain splitting (ADS) method is applied as an indicator to characterize the dynamical structure and nonlinearity of the orbital motion from a new perspective, which is instrumental in robust mission design. The uncertainties of the C_{20} and C_{22} terms in the gravitational potential are considered as these harmonic terms are usually dominant. Asteroid Steins is taken as an example. The relation among the required accuracy, the expansion order and the integration time by applying ADS is firstly investigated. Then the effects of the uncertainties of both the gravity and the solar radiation pressure (SRP) perturbation on orbits with different geometries are studied. The orbital motion is found to be more sensitive to the uncertainty of the C_{22} term than that of the C_{20} term. SRP has a significant effect on the high-altitude motion. Moreover, the bounds of the state flow over the uncertainties are also evaluated along with the propagation. The results are validated against numerical integrations and Monte Carlo simulations.

Keywords: asteroid exploration, model uncertainty, automatic domain splitting, dynamical structure, robustness

1. Introduction

Asteroids usually have an irregular gravity field due to their non-spherical shape, which gives rise to highly nonlinear dynamics. Moreover, their gravity fields are

preliminarily modeled with large uncertainties due to the limited availability of ground observations. The solar radiation pressure (SRP) perturbation generally plays an essential role in small bodies' motion. SRP cannot be accurately determined due to an incomplete understanding of the reflection property of all the surfaces of the spacecraft. Consequently, the motion can be highly unstable due to the perturbations of the irregular gravity field and the SRP and cannot be estimated accurately due to their uncertainties. Therefore, identifying regions of the phase space robust to these uncertainties is essential for such missions.

Though the nonlinearity of the dynamics and the stability of motion around small bodies have been extensively addressed [1], the analysis of the effect of the uncertain irregular gravity field and SRP on orbital propagation is limited. Using Monte Carlo (MC) simulation, Melman et al. [2] investigated the effects of Itokawa's uncertain gravity on the evolution of the so-called solar terminator orbit (STO) whose orbital plane is perpendicular to the Sun-asteroid line [1]. The STO was found to be more sensitive to this uncertainty if the gravity of the asteroid is weak. Based on the averaged dynamics and MC simulations, a frozen-STO was found to be more robust against the execution uncertainties or errors than a circular-STO [3] for the small asteroid Bennu with a weak gravity field. By applying the semi-analytical Differential Algebra (DA) method, Feng et al. [4] investigated the effect of uncertainties in Stein's gravity field on the orbits with different geometries. Retrograde orbits were found to be more robust than prograde ones. And polar orbits were found to be more sensitive to these uncertainties. This study extends the previous research by investigating the effects of uncertainties of both the irregular gravity and the SRP on motions with highly nonlinear dynamics using ADS.

Generally, the uncertainties are propagated with two main approaches, the linear ones, and the nonlinear ones. For the former type, the state transition matrix (STM) is usually applied, which maps the deviation of the initial state of a trajectory to that of the final state. Eigenvalues of the STM indicate the linear stability of this trajectory [5]. For the latter type, many different methods were developed to address the deficiency of the linearization. The MC method is a purely numerical method that

2

performs pointwise simulations of the fully nonlinear dynamics, providing true trajectory statistics. However, it is computationally intensive, and the computational time increases with the increasing number of samples [6]. More efficient methods include the unscented transformation (UT) [7], the Gaussian mixtures model (GMM) [8], and the polynomial chaos expansion (PCE) [9], which are also sample-based methods. They are also classified as non-intrusive methods as they do not require access to the details of the dynamical equations, which are treated as a black box. An alternative way to deal with the nonlinearity is approximating the flow of the dynamics in Taylor or polynomial series, i.e., the DA method and the general polynomial algebra (GPA) method [10], respectively. These methods require explicit knowledge and treatment of the system's dynamical equations and are categorized as dynamic-based or intrusive methods. The DA method computes Taylor expansions of the flow up to an arbitrary order with automatic differentiation [11]. Then pointwise propagations are performed in the DA framework by the fast evaluation of the Taylor polynomials instead of running thousands of pointwise integrations as in the MC method. Consequently, the computational time is reduced considerably, while the accuracy can be tuned by adjusting the Taylor expansion's truncation order. DA has been applied widely in orbital dynamics, e.g., asteroid encounter analysis [12] and orbit conjunction analysis [13].

For the sample-based methods, the main drawbacks are that the number of samples (e.g., UT) and the number of expansion terms (e.g., PCE) change linearly and exponentially, respectively, with the dimension of input uncertainties, which is computationally expensive for large-dimensional uncertainties of complex systems. On the other hand, the dynamics-based methods are local and can barely handle dynamics with a large uncertainty set. They are also computationally intensive for high-order approximations of a high-fidelity system. For instance, DA fails when the high nonlinearity of the dynamics, the large initial uncertainty set, and long-term propagation prevent good convergence of the Taylor expansion, and a single Taylor expansion of the flow is not accurate enough to map the entire initial uncertain domain. Therefore, to apply these methods on motions with highly nonlinear

dynamics and large uncertainties, these drawbacks need to be overcome.

The ADS method was introduced to solve the above issue by automatically splitting the initial uncertain domain into two equal sub-domains whenever the Taylor expansion's truncation error reaches a predefined threshold. ADS was firstly introduced by Wittig et al. [14], where it was applied to the orbital propagation of asteroid (99942) Apophis considering its initial state uncertainty. The non-impact and close-encounter regions of Apophis' state-space with respect to Earth were identified and validated against pointwise simulations. It was also demonstrated that ADS can infer the system's dynamical behavior over the initial uncertainty domain through the resulting splitting structure at the end of the propagation. Precisely, the region of frequent splits corresponds to the dynamics' strong nonlinearity and is automatically identified by the algorithm. More details of ADS are given in Section 2.

In terms of dynamical structure, several indicators have been widely applied. For instance, the Lyapunov Characteristic Exponent (LCE) is obtained from the STM's eigenvalues of an autonomous system [15]. Zero values of LCE indicate that the neighboring of this trajectory is bounded, and the positive values of LCE imply that the neighboring trajectories deviate exponentially from the nominal one. Another indicator is the so-called Lagrangian Coherent Structure (LCS) [16]. It is defined from the Finite-time LCE (FTLE) that measures the divergence rate of trajectories flowing from neighboring initial conditions. More specifically, LCSs are determined by the ridges of the Finite-time LCE field of a time-dependent system that partition the phase space into coherent dynamic behavior regions. However, LCS is computationally intensive for systems with dimensions higher than four. The Jet Transport method, which is based again on polynomial algebra, was demonstrated to be capable of detecting different dynamic regimes in autonomous and non-autonomous dynamical systems by identifying the separatrices of the pendulum and the invariant manifolds of the circular restricted three-body problem [17]. In this study, ADS is used as an alternative indicator of the dynamical structure of a highly nonlinear system with uncertainties, focusing on the stability, robustness, and boundedness of the associated motion. One advantage of this indicator is its capability of dealing with

4

uncertain dynamics, which is very different from the previous indicators that work with deterministic dynamics.

As explained previously, the irregular gravity and the SRP, together with their uncertainties, are the perturbations considered in the dynamical modeling. In real mission operations, the gravity field of a small body is usually determined in terms of spherical harmonics that are a generalized representation of an arbitrary gravity field. In addition, the spherical harmonics model is usually applied to mission/orbit design. Therefore, the irregular gravity in this research is represented by the spherical harmonics model. For the gravitational field represented by mascons and polyhedrons, this research can also be directly applied, as long as the distributions of uncertainty parameters in these gravitational models are available. Recent research [18] shows that the spherical harmonics model provides a way to quantify the uncertainty of a given stochastic polyhedron model. In particular, since the C_{20} and C_{22} terms are generally dominant terms of the irregular gravity, their uncertainties are believed to contribute to the major impact on the orbital motion and are the only harmonic terms whose uncertainties are considered in this study. Nevertheless, it is straightforward to generalize this research to consider the uncertainties of higher-order harmonic terms, especially for the situation of highly irregular bodies. As far as the authors know, this is the first research in which ADS is applied to investigate the effect of model uncertainties on motion dynamics around small bodies.

The paper is organized as follows. First, we introduce the basics of using ADS as a stability indicator and its comparison with the FTLE for a simple pendulum model. Second, the dynamics of orbital motion around an asteroid is modeled, and the DA algorithm is applied to expand the dynamical flow to high orders with respect to the gravity uncertainty for the example asteroid Stein. Third, by applying ADS, the sensitivity of orbits with different geometries to the gravity uncertainty is systematically investigated, together with validation against numerical simulations. By including the SRP, its additional effect on the motion's stability and robustness is investigated. Finally, we conclude this study and gives prospects for future work.

2. Automatic Domain Splitting as a dynamical indicator

This section first introduces the ADS methodology in detail and then analyze its feasibility as a dynamical indicator with its first application to a simple pendulum.

2.1 The ADS methodology

As already mentioned in Section 1, the DA method computes Taylor expansions of the flow of the dynamics up to arbitrary orders with automatic differentiation. The main idea of the ADS is to determine the time epoch when the flow expansion over a given initial set is not capable of describing the dynamics with the required accuracy anymore, by applying an automatic algorithm. Once this situation is detected, the domain of the original Taylor expansion is divided into two sub-domains of the same size along one of the expansion variables. Then the dynamics is re-expanded with respect to the new center points of these two sub-domains, respectively, giving rise to two separate Taylor expansions. This process is illustrated in Fig.1, in which the error is the truncation error, and it is an absolute value that measures the difference between the n+1 time differentiable function and its Taylor expansion of order n. The ε is the required accuracy. Following such a split, in each subdomain the integration continues in the same manner until further splits are required or the final integration time is reached. For the numerical integration, the DA framework applies the Dormand–Prince Runge–Kutta 7/8 scheme with the 7th order solution for step size control and the 8th order solution for propagation.
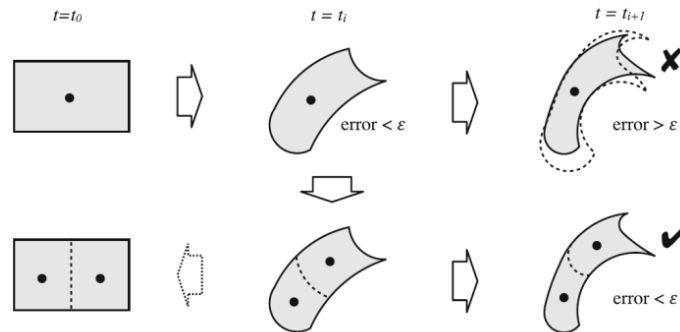
Figure 1 Illustration of the propagation process with ADS [14]

Specifically, all splits are performed in the direction that contributes the most to the truncation error of the Taylor expansion, resulting in the maximum reduction of this error. During the propagation, the splitting can occur along all directions, but predominantly along these directions to which the dynamics is more sensitive. The

final result is a list of Taylor polynomials of the final state, each of which describes the evolution of each sub-domain. Therefore, the set of all Taylor polynomials accurately maps the entire initial domain into the final domain. A minimum domain size is set at the beginning of the integration. Consequently, it is possible that some sub-domains cannot reach the final integration time as they reach the minimum allowed size earlier. These sub-domains are shown to correspond to regions of strong nonlinearity of the dynamics, which are automatically identified by the algorithm. In addition, ADS is capable of accurately propagating large sets of uncertainties in highly non-linear dynamics. The reader can refer to Wittig et al [14] for more detailed description and demonstration about ADS.

2.2 Using ADS to detect structures of a dynamical system

As indicated in Section 2.1, the earlier the first split occurs, the stronger the nonlinearity of the dynamics is. The nonlinearity is closely related to the stability and robustness of the motion; i.e., an unstable motion tends to be characterized by strong nonlinearities either on the state or on the dynamical model parameters, which make it more sensitive and less robust to uncertainties. Therefore, the first split time of the ADS can be used to detect the overall dynamical structures of a nonlinear system and also the transition among different structures. This study explores the feasibility of its application to orbital motions around small bodies that are characterized by highly nonlinear and uncertain dynamics. As a straightforward test of this idea, the approach is first used to investigate the dynamical structure of a simple pendulum system.

2.2.1 Detection of the dynamical structure of a simple pendulum

As discussed in Section 1, the FTLE is an efficient tool to address the stability or chaoticity of the nonlinear dynamics. To investigate the capability of ADS detecting dynamical structures, we first apply it to a simple pendulum model and compare its performance with that of the FTLE. The dynamics of the simple pendulum is given as

$$
\begin{cases}
\dot{\theta} = \xi \\
\dot{\xi} = -\dfrac{g}{L}\sin(\theta)
\end{cases}
$$

7

Given $L = g$, the numerical FTLE field of this model at time t=20 from [19] is given in the left plot of Fig.2. It is evident that the red separatrix region has the largest FTLE value, indicating the high divergence rate of the dynamics in this region. On the contrary, the blue region has the smallest FTLE value and has relatively better dynamical stability. Therefore, this FTLE value characterizes the dynamical structure of the phase space of a simple pendulum.

As described in Section 1, for the DA-based ADS method, all the evaluations can be carried out in the DA framework by computing the expansion flow of a general ODE to arbitrary order with respect to the initial conditions. Given a general dynamical system

$$\begin{cases} \dot{X} = f(X, t) \\ X(t_0) = X_0 \end{cases}$$

with state $X = (x_1, x_2, \ldots x_i \ldots)$ and (for instance) uncertain variable x_i, to obtain the high-order expansion of the phase flow, the first step is to initialize x_i as a DA variable

$$[x_i] = x_i + \delta x_i$$

where δx_i represents the displacement from the nominal value x_i. Then the dynamics is expanded in Taylor series with respect to x_i in the DA framework. Therefore, to apply ADS to this pendulum model, the two variables θ and ξ are first initiated as DA variables as

$$\begin{cases} [\theta] = \theta_{mean} + 3\sigma \cdot \delta\theta \\ [\xi] = \xi_{mean} + 3\sigma \cdot \delta\xi \end{cases}$$

in which the 3σ of the assumed Gaussian distribution is 3×10^{-2}. The map of the first split time on the $\theta - \xi$ plane is obtained as the right plot of Fig.2. It is seen that the dark red region and the bright region have the shortest and longest first split time, respectively, indicating the relatively high and low nonlinearity of the dynamics in these regions. In addition, they also correspond to the separatrix and the oscillation region, respectively, showing that the dynamical structure of the phase space can be detected. Since the structure of the map of the first split time from ADS coincides with that of the FTLE plot for the same dynamical model, ADS is capable of capturing the

1 dynamical structure of the system similarly to FTLE. In the following sections, we

2 further explore this possibility by studying the dynamics of motion around asteroids.
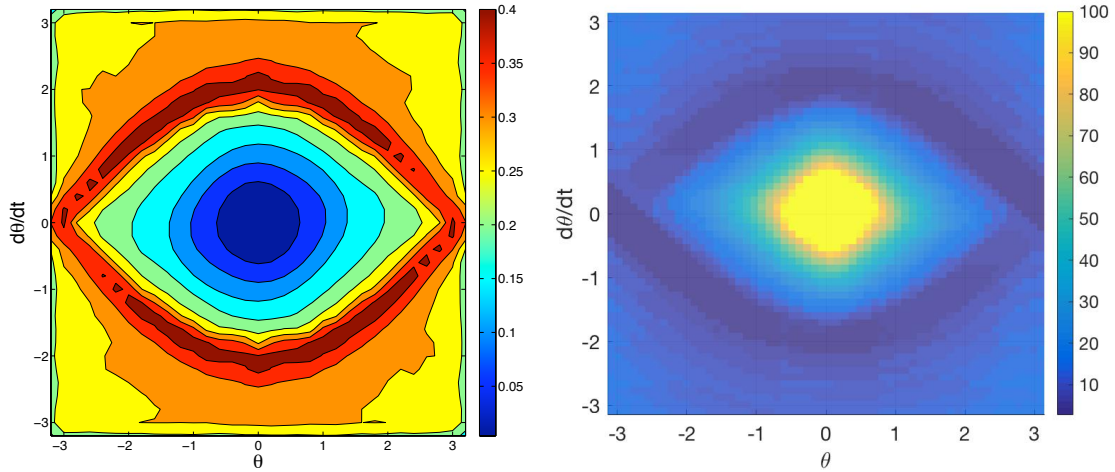
3

4 Figure 2 left: Numerical FTLE field for the simple pendulum model from Ref [19]; right:

5 map of the first split time obtained with ADS in the same region.

3. Dynamics with irregular gravity

7 To separate the analysis of the effects of uncertain gravity and uncertain SRP on the

8 orbital motion, in this section, we consider only the irregular gravity and its

9 uncertainty in the simulation. The effect of the SRP perturbation is investigated in

10 Section 4.

3.1 Dynamical Modeling

12 The equation of motion for an object located at $\vec{r} = (x, y, z)$ in the vicinity of an

13 asteroid in the inertial frame is given as [1]

14
$$\ddot{\vec{r}} = \frac{\partial U}{\partial \vec{r}} \tag{1}$$

15 where U is the gravitational potential of the small body in the inertial frame. The

16 gravitational potential is represented in spherical harmonics as [9]

17
$$U_a = \frac{GM}{r} \left\{ 1 + \sum_{n \geq 2}^{\infty} \sum_{m=0}^{n} \left(\frac{R_e}{r} \right)^n P_{nm}(sin\theta)[C_{nm}cos(m\lambda) + S_{nm}sin(m\lambda)] \right\}$$

18 where GM is the gravitational constant of the small body; R_e is the reference radius

19 of the small body that is usually defined as half of the largest dimension of the whole

body; r, θ and λ are spherical coordinates from the center of mass to a given point P in the body-fixed frame (i.e., the radial distance $|\vec{r}|$, latitude and longitude, respectively); P_{nm} is the associated Legendre polynomial; C_{nm} and S_{nm} are the spherical harmonic coefficients that are determined by the mass distribution within the body. However, U_a is defined in the body-fixed frame of the small body, and it is transformed to the inertial frame (denoted as U) for the integration in the following simulations. This study uses gravity field truncated at the 4th degree and order, which captures the main characteristics of the whole gravity and meanwhile reduces the computational effort.

As discussed in Section 1, this study focuses on investigating the effect of the uncertain C_{20} and C_{22} terms on the state propagation, i.e., parameter uncertainties. Given a general dynamical system

$$\begin{cases} \dot{X} = f(X, p, t) \\ X(t_0) = X_0 \end{cases}$$

with the vector $p = (p_1, p_2, .. p_n)$ including all the uncertain parameters of the dynamical model, to obtain the high-order expansion of the phase flow, the first step is to initialize p as a DA variable as

$$[p] = p + \delta p$$

The vector $p = (C_{20}, C_{22})$ can be initialized as a vector of DA variables as

$$\begin{cases} [C_{20}] = C_{20} + \delta C_{20} \\ [C_{22}] = C_{22} + \delta C_{22} \end{cases}. \tag{2}$$

Readers can refer to Ref [4] for more details about modeling the uncertainty of the gravity field.

3.2 Uncertainties of the C20 and C22 terms

Asteroid Stein is used as the test case. Due to its size and mass, the orbital motion around it is possible [1]. Its physical parameters are given as [2, 8]

$$GM = 7.7 \times 10^{-6} \, km^3/s^2, R_e = 3.35 km, T_{period} = 6.047h$$

$$C_{20} = -9.78 \times 10^{-2}, C_{22} = 1.32 \times 10^{-2} \tag{3}$$

in which GM, R_e and T_{period} are the gravitational constant, reference radius and rotation period of Stein, respectively. C_{20} and C_{22} are the second order and degree of

1   the irregular gravity of Stein. Its gravity harmonic coefficients up to the 4th degree and

2   order are listed in the Appendix and are included in the dynamics. We assume both

3   the C_{20} and C_{22} terms have a Gaussian distribution with their mean values given in Eq.

4   (3). From Rosetta's flyby of Stein, the 1σ uncertainties of these two terms are

5   estimated to be 6.3×10^{-3} [2]. However, since the modeling of the gravity can be

6   improved significantly during the approach phase of the mission, a reduced value of

7   6.3×10^{-5} is used here to assess the effect of gravity uncertainty on the orbital motion.

8   In addition, we assume that there is no correlation between the uncertainties on C_{20}

9   and C_{22}. Moreover, the 1σ uncertainty of Stein's central gravity GM is not considered

10 here as it is generally three orders of magnitude smaller than that of the second-order

11 gravity term. In the following simulations, the unit gravitational constant and the unit

12 length are defined as GM and R_e, respectively, and the other variables are scaled or

13 normalized accordingly.

14 **3.3 Splitting on the C$_{20}$ - C$_{22}$ domain with ADS**

15 As a first step, the relation between the expansion order and the accuracy of the Taylor

16 polynomials, the relation between the splitting precision required by ADS and the

17 number of splits, as well as the computation time are investigated. The precision ε is

18 defined as the limit when a split is triggered.

19   First, the C_{20} and C_{22} terms are initialized as DA variables with their 1σ uncertainty

20 6.3×10^{-5} as

21
$$\begin{cases} [C_{20}] = -9.78 \times 10^{-2} + 3\sigma \cdot \delta C_{20} \\ [C_{22}] = 1.32 \times 10^{-2} + 3\sigma \cdot \delta C_{22} \end{cases} \tag{4}$$

22   Results are compared for different precision ε (10^{-4}, 10^{-7} and 10^{-10}) and different

23 Taylor expansion orders (5th, 7th and 10th). The domain splitting on the C_{20}-C_{22} plane

24 is given in Fig.3 for the circular orbit with a=1.98 and for the integration time of 10

25 orbital periods (i.e., t=10P). It can be seen that the lower the truncation order and the

26 higher the required precision (i.e., the smaller the required truncation error), the

27 more splits occur in the initial domain, due to the fact that low order Taylor

28 expansions fail to approximate the dynamics with sufficient accuracy over larger

domains. Moreover, since all the splits occur along the direction of the C_{22} term, it is concluded that the motion is more sensitive to the variation of this term.
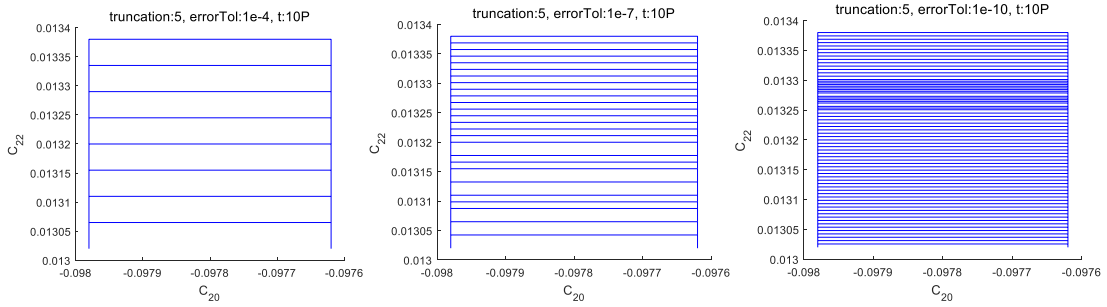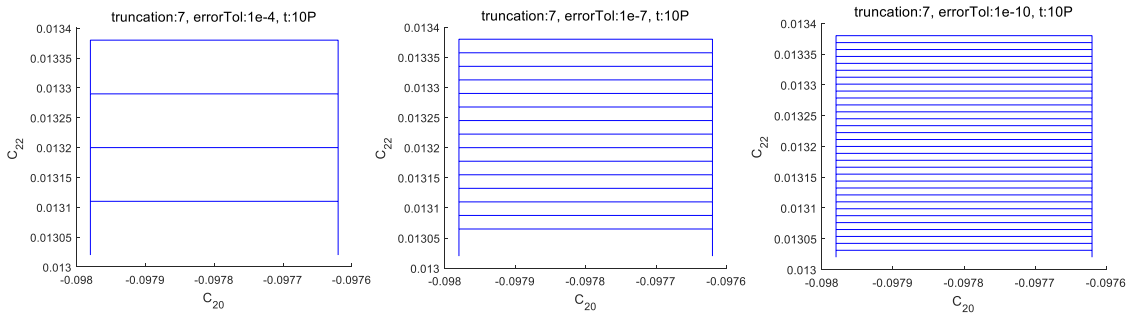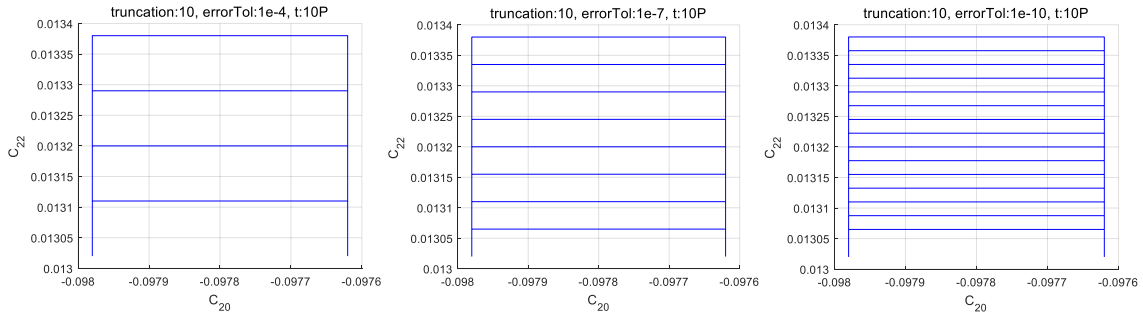

Figure 3 The domain split on the C_{20} -C_{22} plane for a=1.98 and t=10P (i.e. 10 orbital periods) at the truncation order 5, 7 and 10 from top to bottom and for error tolerance 10^{-4}, 10^{-7}, 10^{-10} from left to right.

Fig.4 gives the computational time as a function of the precision ε and expansion order. The 10th-order requires the longest computational time for precisions larger than 10^{-6}. However, the computational time required by a 10th-order propagation reduces significantly for precisions smaller than 10^{-8}. This phenomenon can be explained by the fact that higher-order expansions generally require more time than low-order expansions if both of them could meet the accuracy requirement. To better balance the computation time and accuracy, a precision of 10^{-10} and 10th-order

1 propagations are applied in the following simulations.
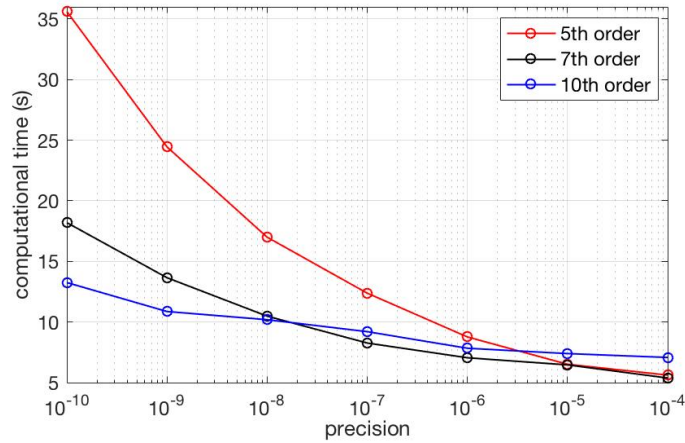
3 Figure 4 The relation between the expansion order and time consumption for

4 different precisions

3.4 Numerical simulations and analysis

6 Due to constant distance from the small body, a circular orbit is generally preferred

7 for mission operations [20]. This is the case studied in this research. For a given orbit

8 inclination, the ascending node Ω and $u = \omega + f$ (i.e., the argument of latitude)

9 fully describe the orientation and the position of the initial point on this circular orbit,

10 respectively. For a circular orbit, u actually coincides with the true anomaly f, as

11 there is no specific definition of ω. The effect of the uncertain gravity field on

12 different orbital geometries is analyzed.

3.4.1 Map of the first split time on the *a-i* plane

14 First, the effects of orbital elements a and i are investigated by dividing the *a-i*

15 plane ($a \in [1, 3]$, $i \in [0, 180°]$) into a 100×100 grid. Given $\Omega = u = 0$ and for the

16 integration duration t=1000, the first split time of each orbit is recorded on the *a-i*

17 plane, as shown in Fig.5, which displays complicated dynamical structures. The deep

18 blue region shows that the split occurs shortly after the integration starts, and the

19 yellow region shows that the integration is performed without any split. For ADS, the

20 sooner the first split occurs, the stronger the nonlinearity of the dynamics. Therefore,

21 Fig.5 indicates that the motions close to the asteroid show stronger nonlinearity than

22 those far away from the asteroid, due to the stronger perturbations of the irregular

1   gravity field in its vicinity. The indications of this map on the stability and robustness

2   of orbital motion will be investigated by numerical integrations and uncertainty

3   propagation in the following sections.

4
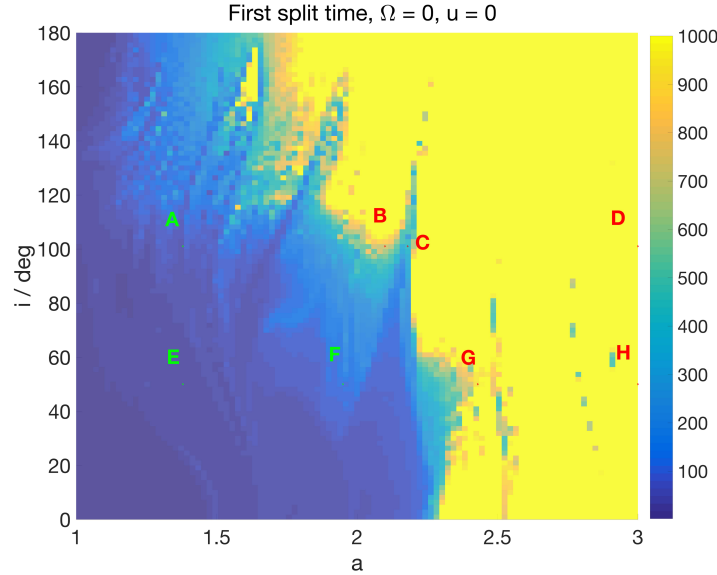
Figure 5 The first split time on the *a-i* plane with 1σ uncertainty of 6.3×10^{-5} of both the C_{20} and C_{22} terms.

3.4.2 The effect of u on the first split time

8   In this section, we investigate the effect of $u = f$ on the first split time. To focus on

9   the influence on the highly nonlinear region in Fig.5, the simulation is performed only

10   in the range $a \in [1, 2.5]$. To clearly illustrate the 4-dimensional matrix that includes

11   a, i, u and the first split time, several slices are selected and shown in Fig.6. In Fig.6A,

12   the five slices represent the *a-i* plane at u = 0°, 45°, 90°, 135° and 180°, respectively.

13   It is seen that on both planes of u = 0° and 180° (i.e. with the motion starting from

14   the equatorial plane) there are larger blue regions than that on other planes. The

15   largest yellow region appears on the plane of u = 135° as indicated by the red dash-

16   dot circles. As a comparison, the same regions are marked by the dark dash-dot circles

17   on other planes but they are not yellow anymore. However, in spite of these

18   differences, the general structure stays nearly the same for different values of u. This

19   is understandable as we generally study similar orbits when keeping i, Ω fixed and

20   varying u in [0°, 180°].

14

1   In Fig.6B, the slices represent the *i-u* plane at a = 1, 1.5, 2, 2.5. Though significant

2   variations appear on the slices with the variations of a and i , there is very small

3   difference along the direction of *u* for almost all these planes. This indicates that the

4   influence of *u* is negligible. In Fig.6C, the slices represent the *a-u* plane at i = 0°, 60°,

5   120°, 180°. For i = 0° and 180° the dynamics is slightly sensitive to the initial u, due

6   to the effect of the C_{22} term that represents the non-uniform mass distributions in the

7   longitude direction. This phenomenon is consistent with the results of our previous

8   study about the effect of Ω [4]. Therefore, we can conclude that the motion under

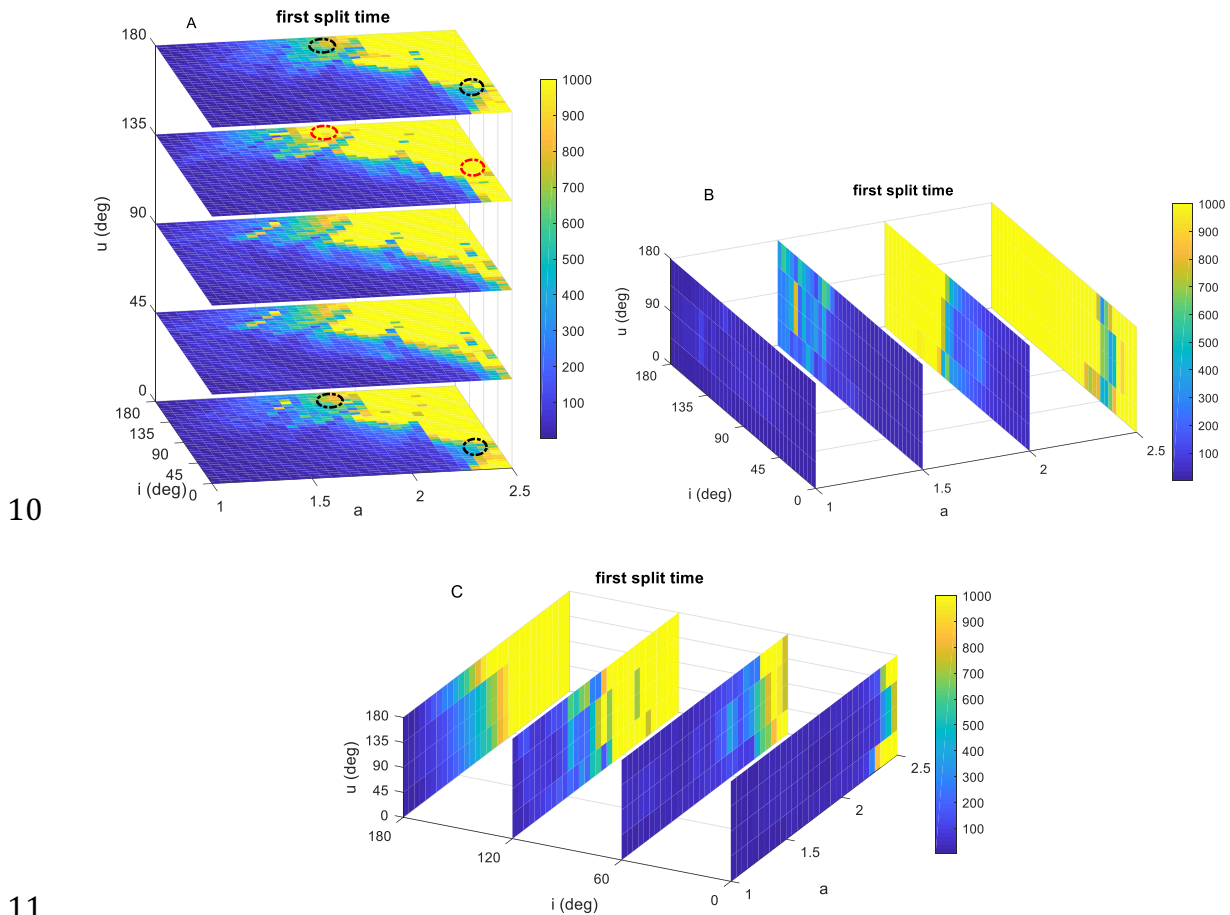9   gravity uncertainty is more sensitive to the orbital elements a and i.

10

11

12   Figure 6 The slices of the first split time in the *a-i-u* phase space.

13   **3.4.3 Numerical integrations**

14   To get a straightforward insight on the dynamical structure revealed by Fig.5, sample

15   orbits are selected from the blue and yellow regions, respectively, for numerical

15

1 integrations. The initial conditions of these orbits are summarized in Table 1.

2 Table 1 Initial conditions of sample orbits with $e=\omega=\Omega=f=0$

| orbits	A	B	C	D	E	F	G	H
a	1.38	2.10	2.18	3	1.38	1.95	2.43	3
i	101°	101°	101°	101°	50°	50°	50°	50°

3   For all these circular sample orbits, the two-body initial conditions are used for the

4 integrations. The propagation duration is set to 400, rather than 1000 as the orbits in

5 the non-yellow region diverge significantly in a short period of time. The evolutions

6 of their orbital elements a, e, i, are illustrated in Figs.7 and 8.

7   It can be seen that orbits A and E from the deep blue region have the largest

8 variations of e and i, respectively, compared with the simulated orbits with the same

9 inclinations. This indicates their strong instabilities, due to the fact that both A and E

10 are extremely close to the asteroid and are strongly perturbed by the irregular gravity

11 field. For orbits B, C, D, G and H, the evolutions of their orbital elements are much

12 better bounded, demonstrating that they are more stable than A and E. In addition, it

13 is apparent that the retrograde motion (orbit A, B, C, D) is generally more stable than

14 the prograde one (orbit E, F, G, H), in terms of the magnitude of the variations of $a, e,$

15 i. For instance, by comparing orbit A with orbit E, the latter demonstrates stronger

16 instability as a and e vary significantly up to 5.6 and 0.8, respectively, which would

17 lead to an impact with the asteroid. In addition, their inclination oscillates by 20

18 degrees. The same orbital parameters for orbit A are better bounded. These

19 phenomena are in agreement with the conclusion in [1] and are also visible from the

20 difference of the top and bottom regions of Fig.5. These numerical integrations

21 validate the dynamical structure of Fig.5 and show that the first split map is capable

22 of indicating stability.
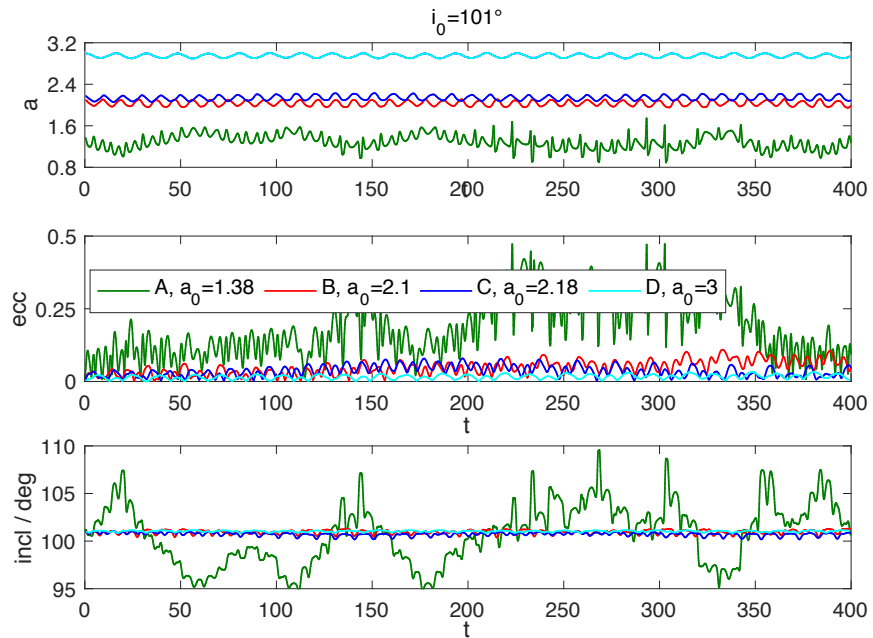
1

2   Figure 7 The evolutions of *a, e, i* for orbits A, B, C and D with the same inclination of

3   101°
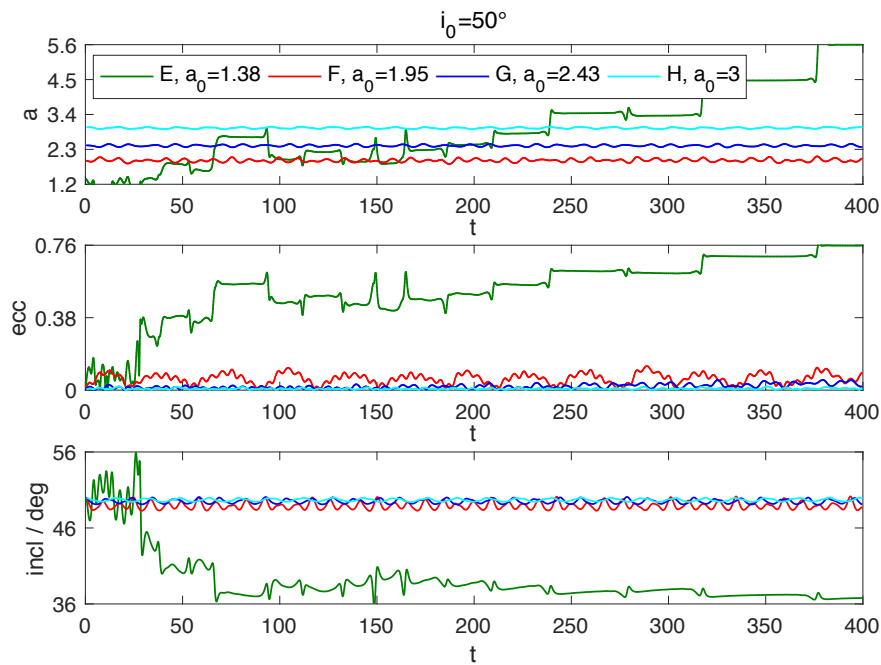
4

5   Figure 8 The evolutions of *a, e, i* for orbits E, F, G and H with the same inclination of

6   50°

7   **3.4.4 Uncertainty Propagation**

This section investigates the robustness of the motion by studying the evolution of the bounds of the spacecraft distance from the asteroid. The distance of the nominal trajectory from the asteroid is denoted the reference distance.

For all the same sample orbits, two simulations are performed. One is by applying the MC method to propagate the gravity uncertainties with 100 samples. The other is by computing the bounds of the uncertainty set through the Taylor expansion of ADS. For the latter, once the high-order Taylor expansion with respect to the initial uncertainties is obtained, the outer bound of the range of the expansion at different times is then estimated by applying interval arithmetic [21]. However, the computed bounds might overestimate the true range of the Taylor polynomial. In addition, to ensure the accuracy of the estimated bounds, the Taylor expansion needs to be accurate in the whole uncertainty domain.

For low-altitude orbits with a=1.38, the integrations already diverge significantly before reaching t=400. Therefore, their MC simulations (black lines) are truncated at t=300 for orbit A with i =101° and at t=76 for orbit E with i =50°, which are displayed in the first two subplots of Fig.9. The evident divergences from the reference distance (red lines) occur from about t= 240 for the retrograde orbit and t=60 for the prograde one. This result indicates that the retrograde motion is more robust than the prograde motion for the low-altitude orbit. In addition, the estimated lower and upper bounds of the Taylor expansion of the two orbits are also displayed in the lower two subplots of Fig.9, truncated at t=140 for orbit A and at t=45 for orbit E. The green and pink lines represent the upper and lower bounds, respectively. The bounds are found to agree with the MC simulations very well until the single Taylor expansion is not accurate enough over the whole uncertainty domain of the C_{20} and C_{22} terms and the split of the domain is required. Improved bounds based on the Taylor expansions of these split trajectories can be well estimated; these are not displayed here as the main purpose of the current study is investigating the feasibility of the ADS as a dynamical indicator. Nevertheless, in spite of the overestimation, the size and the evolution tendency of the uncertainty domain are well estimated. In addition, the uncertainty set evolves in a highly nonlinear way due to the nonlinear dynamics. The obtained

18

1   evolution of bounds provides a quantitative information to select trajectories that are

2   sufficiently robust to uncertainties.

3
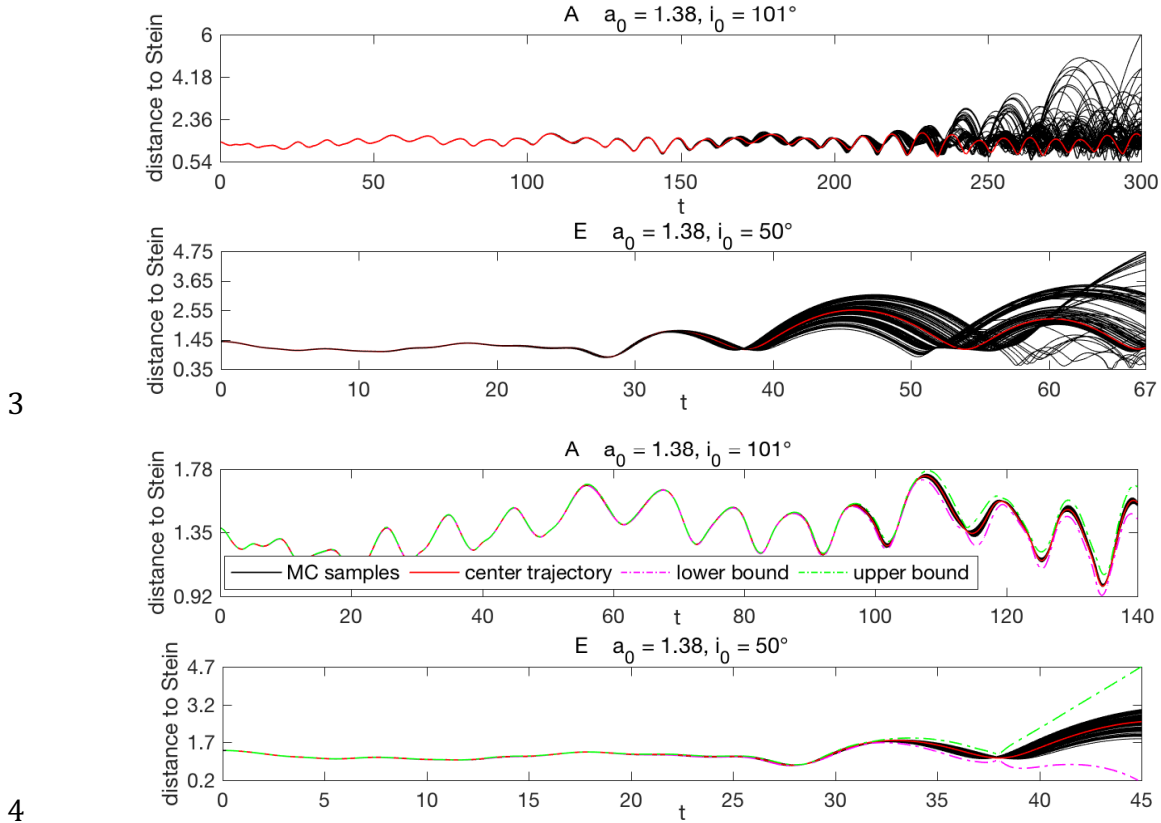
4

5   Figure 9 The distance from Stein of the center trajectory (red solid line), the MC

6   simulations (black solid lines) and the estimated bounds (green and pink dash lines)

7   for orbits A and E.

8

9   In Fig.10, the estimated bounds and the MC simulations of the other sample orbits are

10   illustrated. All the retrograde orbits with $i =101°$ show good robustness as the MC

11   simulations stay extremely close to the reference distance. In addition, the estimated

12   bounds agree very well with the MC results. For prograde orbits with $i =50°$, the one

13   with the smallest semi-major axis (orbit F) shows the highest sensitivity, which is

14   evident from the larger deviations of the MC simulations from the reference distance

15   profile. The other two orbits G and H (further away from the asteroid) also show good

16   robustness. In summary, orbits A, E and F located in the deep blue region in Fig.5 are

17   demonstrated to be more sensitive to perturbations than orbits B, C, D, G and H that

1   are taken from the light blue and yellow regions. In addition, though orbits A, B, C and

2   D have the same inclination, orbit A is more sensitive to uncertainties due to its

3   closeness to the asteroid. This result proves that the first split map can be used as an

4   indicator of robustness that is closely related to the inclination and distance to the

5   asteroid. The DA-based ADS can provide a fast estimation of the uncertainty set as

6   long as the Taylor expansion meets the required accuracy.

7

8
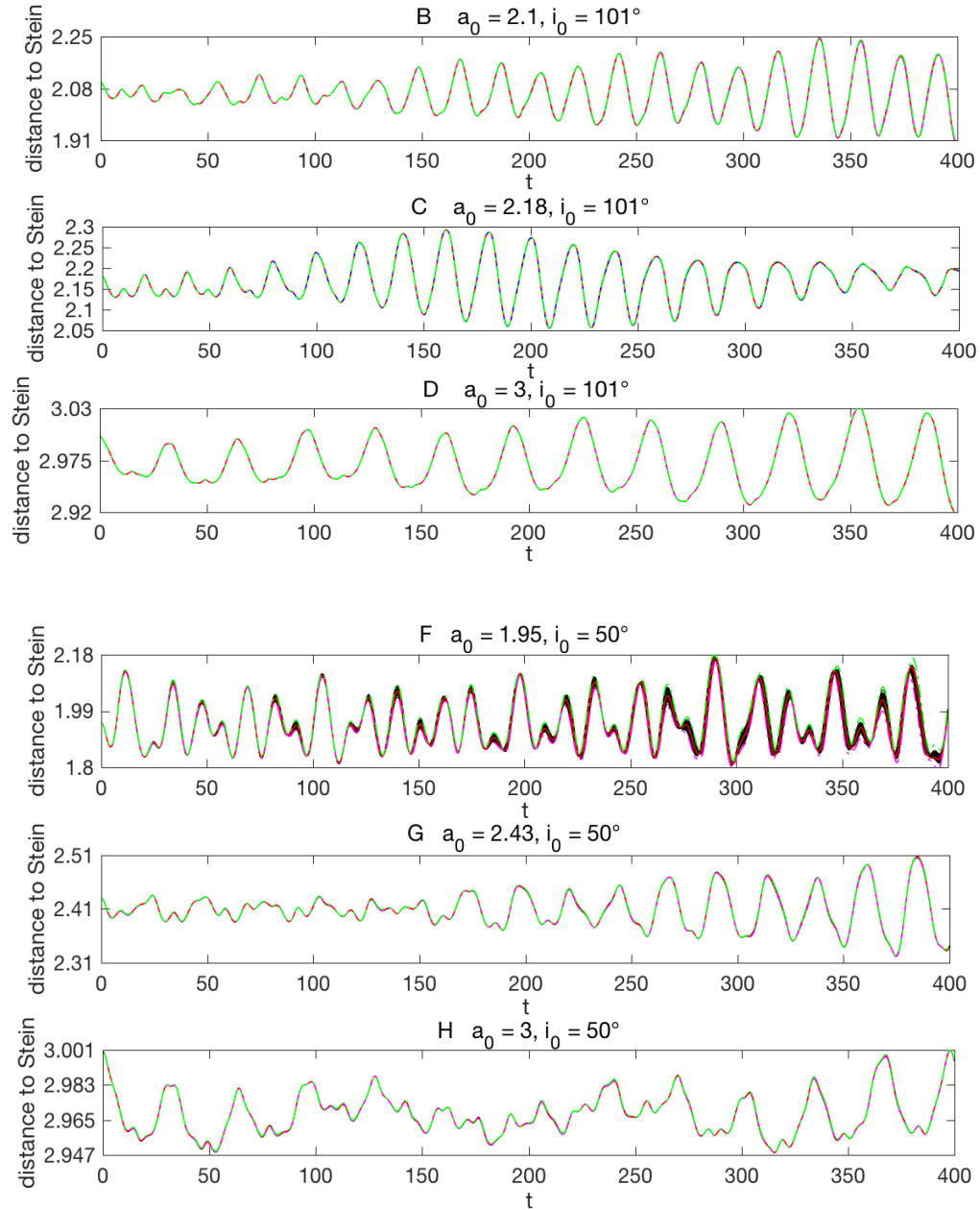
9   Figure 10 Uncertainty propagations of sample orbits B, C, D, F, G and H with an

20

1   integration time of t=400.

2 **3.4.5 The split history of the state flow**

3 To get an insight on the splits of the trajectory, a sample orbit with the initial

4 condition a_0=1.98, i_0= e_0=Ω_0=ω_0=f_0=0° is used. The split history of its orbital elements

5 a and e are given in Fig.11. The black lines represent the evolutions of a and e of the

6 splitting trajectories, and the red lines represent the reference value without

7 considering uncertainty. It is seen that the first split epoch is at about t=47, followed

8 by more and more splits along time, e.g. for $t \in [80, 100]$. There are 84 splits in total

9 that corresponds to 168 splitting trajectories. At the bottom-right corner in Fig.11, i.e.

10 when the split trajectories are closer to the asteroid, it is seen that many more splits

11 are triggered, as the effect of nonlinearity is intensified with time when the motion

12 comes closer to the asteroid. Therefore, the splitting history also indicates the extent

13 of the nonlinearity of the dynamics.
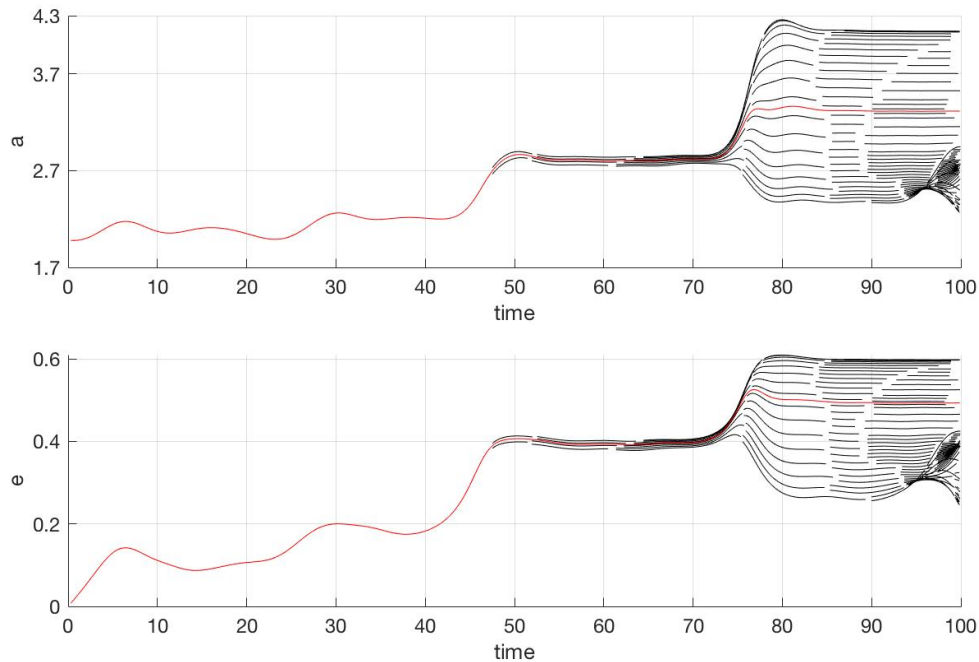
14

15

16   Figure 11 The evolutions of a and e of the orbit integrated with ADS (black) and

17   numerical simulation (red) with the propagation time of t=100.

18

19 **4. Effect of the SRP perturbation**

20 This section first introduces the modeling of the SRP perturbation and then generates

21

1   the map of the first split time considering the SRP. Numerical integrations and

2   uncertainty propagations are performed to validate the dynamical structures.

3   **4.1 Modelling of the SRP perturbation**

4   With the cannonball model, the SRP acceleration on the spacecraft in the asteroid-

5   centered inertial frame is given as

6
$$\ddot{\boldsymbol{r}} = \frac{F_{SRP}}{m} = -(1+\eta) \cdot \rho_0 \varDelta_0^2 \cdot \frac{s}{m} \cdot \left(\frac{\boldsymbol{\varDelta}}{\varDelta^3}\right) \qquad (5)$$

7   in which η is the reflection coefficient of the spacecraft and $\eta = 1$ is for full

8   reflection, s/m is the area to mass ratio of the spacecraft, ρ_0 is the solar radiation

9   flux at the reference distance $\varDelta_0$ (e.g. $\rho_0 = 4.56 \times 10^{-6}$ at distance of 1AU). And

10   $\boldsymbol{\varDelta} = \boldsymbol{r}_\odot - \boldsymbol{r}$ is the relative position vector of the Sun to the spacecraft, as indicated in

11   Fig.12. For the following simulations, the s/m of a general spacecraft is set at 0.01.

12   The distance of the asteroid Stein to the Sun is D_{asteroid}=1.32AU and $\varDelta = |\boldsymbol{\varDelta}| \approx D_{\text{asteroid}}$.
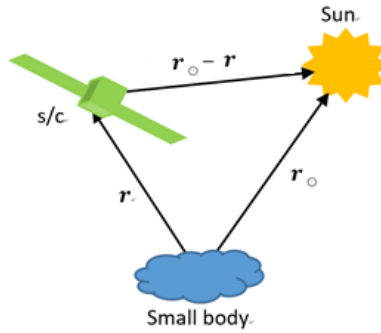
13

14   Figure 12 Illustration of the geometry of the s/c and Sun in the asteroid-centered

15   inertial frame.

16   **4.2 Splitting on the C_{22}-a_{srp} domain**

17   The acceleration due to the SRP is initialized as a third DA variable as

18
$$\begin{cases} [C_{20}] = -9.78 \times 10^{-2} + 3\sigma \cdot \delta C_{20} \\ [C_{22}] = 1.32 \times 10^{-2} + 3\sigma \cdot \delta C_{22} \\ [a_{srp}] = -3 \times 10^{-6} + 3 \times 10^{-6} \cdot \delta a_{srp} \end{cases}$$

19   where a_{srp} is set at the mean value of 3×10^{-6} and varies between its lower and

20   upper bounds, i.e. between -6 $\times 10^{-6}$ and 0, representing an uncertain perturbation

21   force on the spacecraft. Since this study focuses on the simulation in a short period of

22   time, the direction of the SRP perturbation is assumed to be fixed along the x-direction

1   and the orientation of the spacecraft with respect to Sun is also assumed to be fixed.

2   Similarly, the domain splitting on the C_{22}-a_{srp} plane is given in Fig.13 for the

3   integration time of 5 orbital periods (i.e. t=5P). For circular orbit with a=1.98, a_{srp}

4   =3×10^{-6} in the left plot of Fig.13, splits only occur in the C_{22} direction, indicating

5   the gravity uncertainty dominates over that of the SRP. When the mean value of the

6   a_{srp} increases to 3×10^{-5} and it is initiated as

7    $$[a_{srp}] = -3 \times 10^{-5} + 3 \times 10^{-5} \cdot \delta a_{srp}$$

8   more splits occur in the C_{22} direction and the domain splits once in the SRP direction

9   as shown in the middle plot of Fig.13, indicating the stronger nonlinearity of the

10   dynamics for the same orbit by considering larger SRP. However, since the splits in the

11   C_{22} direction are more than those in the SRP direction, the uncertain gravity still

12   dominates the dynamics for the low-altitude orbit with a=1.98. With a larger SRP and

13   increasing the orbit altitude to a=2.2, more splits appear in the SRP direction and only

14   one split appears in the C_{22} direction in the right plot of Fig.13, which shows that the

15   SRP perturbation becomes dominant. These splitting phenomena are consistent with

16   the analysis in [1].
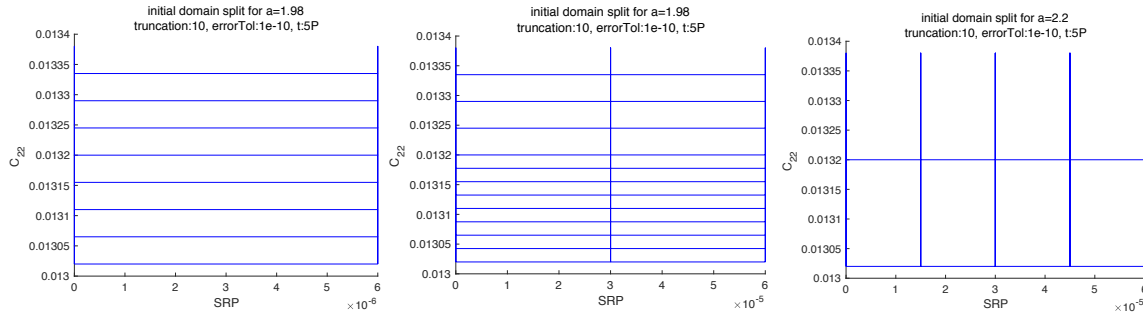
17

18   Figure 13 The domain split on the C_{22}-a_{srp} plane at the truncation order 10 and the

19   error tolerance at 10^-10, for a_{srp} =3×10^{-6} (left) and 3×10^{-5} (middle) at a=1.98,

20   and a_{srp} =3×10^{-5} at a=2.2 (right), respectively, for t=5P.

21   **4.3 Map of the first split time considering SRP**

22   Similarly to Section 3, given $\Omega = u$ =0°, and for the 100×100 grids on the a-i plane

23   ($a \in [1,3]$, $i \in [0,180°]$), the map of the first split time obtained with ADS

24   considering the SRP at a_{srp} =3×10^{-6} is given in Fig.14.

23
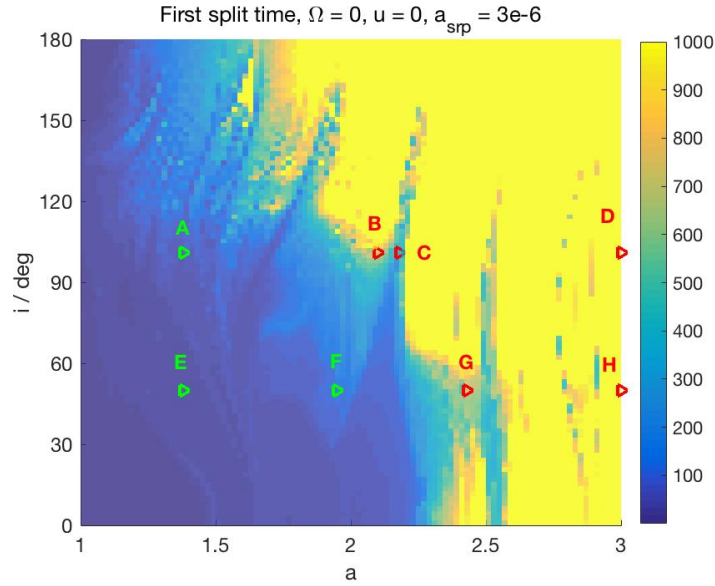
Figure 14　The first split time on the *a-i* plane with 1σ gravity uncertainty of
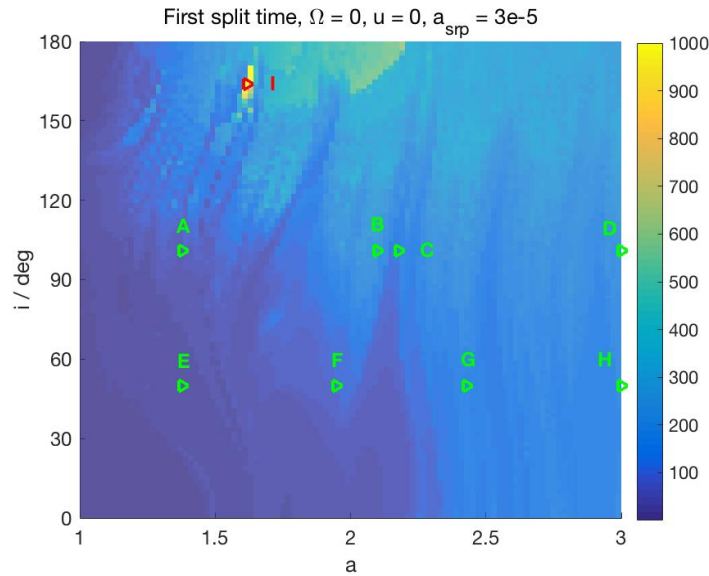
6.3×10^{-5} and the SRP at 3×10^{-6}.

Comparing Fig.14 with Fig.5, it can be seen that they are very similar, indicating that the small SRP perturbation does not affect much the dynamics of orbital motion close to the asteroid. However, the light blue region extends to the areas around $a \in [2.2, 2.4], i \in [0, 30°]$ and $a=2.5, i \in [0, 110°]$, indicating that the SRP destabilizes the motion in these regions. This is consistent with the fact that there are stronger interactions between the SRP perturbation and the gravity perturbation in the middle altitude region [1], since the former and latter ones dominate the high and low altitudes region, respectively.

For objects with large area and small mass, e.g. spacecraft with large solar sails, small particles and dusts, their area to mass ratio is generally large. To investigate the effect of a large SRP perturbation, its mean value a_{srp} is increased to 3×10^{-5} and again the SRP acceleration is initiated as

$$[a_{srp}] = -3 \times 10^{-5} + 3 \times 10^{-5} \cdot \delta a_{srp}$$

The corresponding map of the first split time is given in Fig.15. It is evident that the large yellow region disappears, and it is replaced by the light blue region, meaning that the corresponding motion is destabilized by the dominant SRP perturbation.

24

1 However, the structure of the original deep blue region seems unchanged, as the

2 dynamics is still dominated by the irregular gravity.

3

4 Figure 15 The first split time on the *a-i* plane with 1σ gravity uncertainty of 6.3×10-

5   5 and the SRP at 3×10^{-5}.

6 **4.4 Numerical integrations and uncertainty propagation**

7 To validate the dynamical structure of both Fig.14 and Fig.15, the same sample orbits

8 from Fig.5 are propagated numerically. Their initial conditions can be found in Table

9 1. As shown in Fig.16, for orbits A and E, the SRP significantly perturbs their orbital

10 evolutions from the profiles obtained considering only the irregular gravity. For

11 retrograde orbit A, the large SRP stabilizes the unstable motion perturbed by the

12 irregular gravity field in the close vicinity of the asteroid, by resisting the large

13 variations of *e* and *i* and bounding their variation amplitudes. For the prograde orbit

14 E, the large SRP brings about large variations to *e* and *i,* though the variation of *a* is

15 the smallest. In addition, the obvious deviations of the evolution with SRP from those

16 without SRP happen approximately at *t*=200 for orbit A and at about *t*=60 for orbit E.

17 All these phenomena indicate that the low-altitude retrograde motion is less

18 influenced by the SRP and is relatively more stable to the SRP perturbation than the
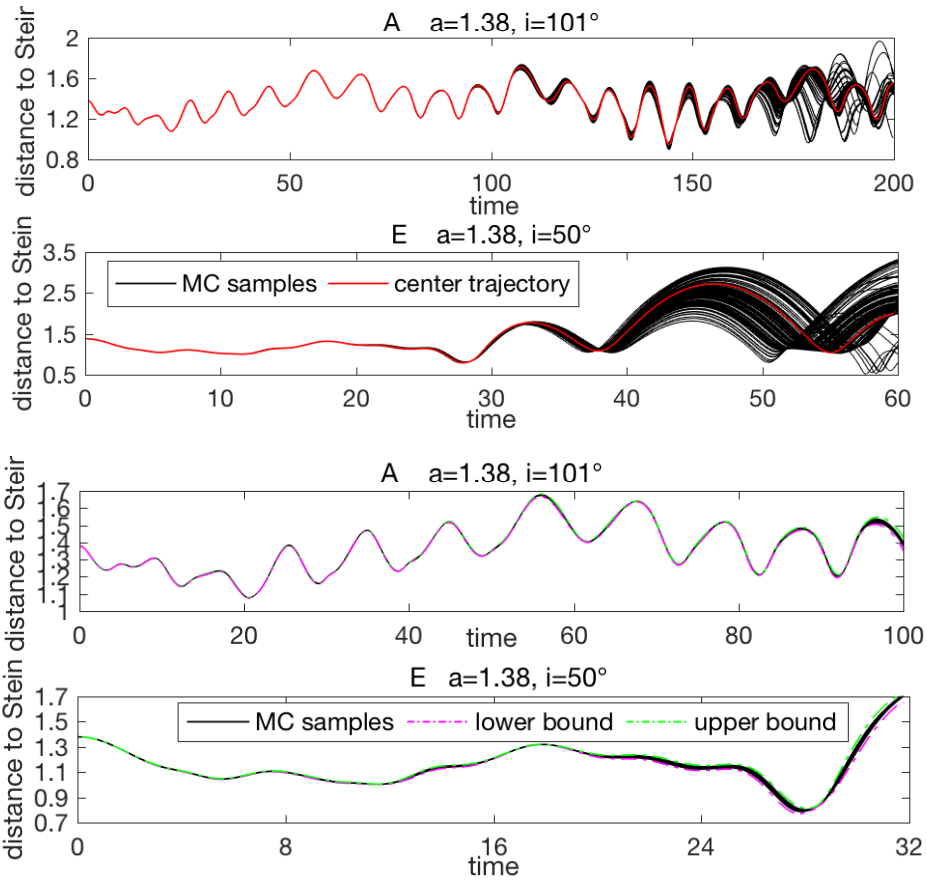
19 prograde motion.
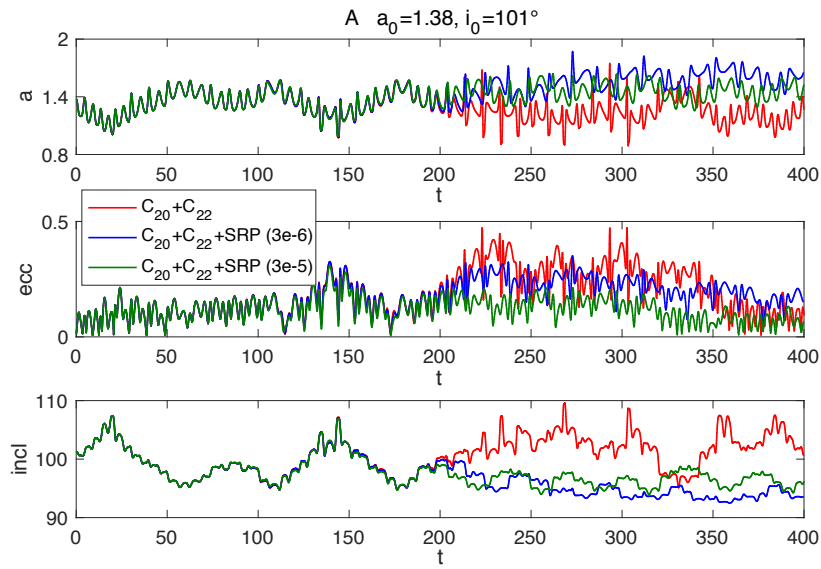
1
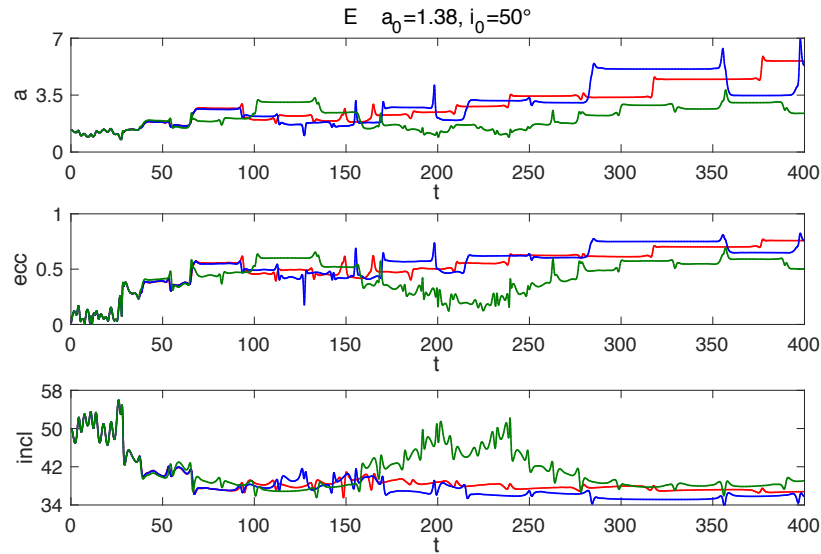
2

3 Figure 16 Evolutions of elements *a*, *e*, *i* for orbits A and E from the deep blue region of

4 Fig.14. The red, blue and green lines represent the dynamics considering only

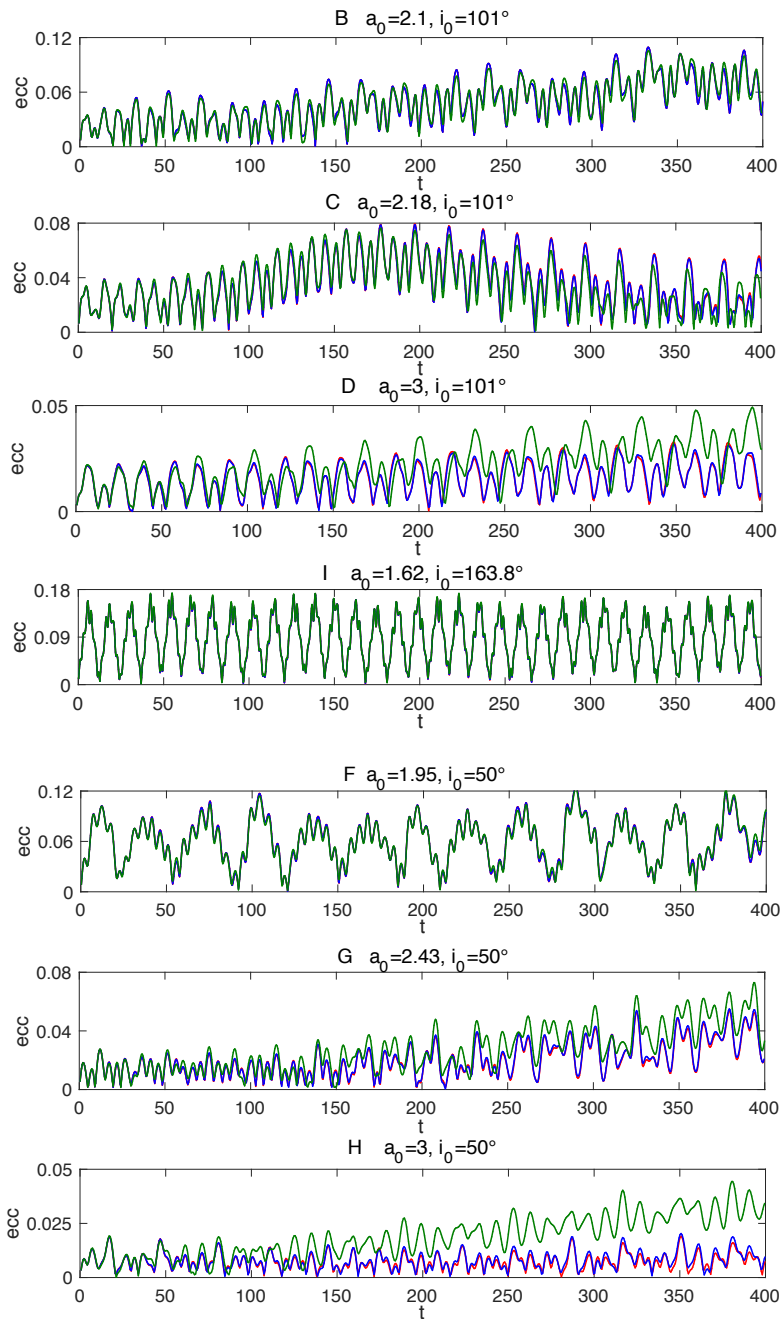5 irregular gravity, small SRP and large SRP, respectively.

Figure 17 The distance to Stein of the center trajectory (red solid line), the MC simulations (black solid lines) and the estimated bounds (green and pink dash lines) for orbits A and E including the SRP perturbation.

The robustness of the sample orbits is also investigated. In the first two subplots of Fig.17 the evolutions of the distances to Stein of orbits A and E are obtained with the MC simulation using 100 samples generated from the given uncertainties of the irregular gravity and the SRP. From the scope of the black lines, it is obvious that the retrograde orbit E is more robustness than the prograde orbit A, especially for longer time. In particular, at t=60, the bounds of the distance of the prograde orbit are between 0.5 and 3.5, whereas those of the retrograde orbit are extremely narrow. Moreover, in the last two subplots of Fig.17 the lower bound (pink line) and the upper bound (green line) estimated from the Taylor expansion are also given for the two orbits before significant overestimations occur. It is seen that they coincide well with the bounds of the corresponding MC simulations for both orbits, and therefore can

27

provide a fast and efficient estimation of the uncertainty set as long as the Taylor expansion meets the required accuracy.

Figure 18 The evolutions of orbital eccentricity of sample orbits B, C, D F, G, H and I. The red, blue and green lines represent the dynamics considering only irregular gravity, small SRP and large SRP, respectively.

For the other sample orbits in Fig.15, the evolutions of a and i are relatively less affected by the SRP than the evolution of e. Therefore, only the evolutions of e are given in Fig.18. For both the retrograde and prograde orbits, the blue and red lines are very close to each other especially for low-altitude orbits, indicating again that the small SRP has very limited effects on the motion. Generally, the deviations of the green lines become larger with the increase of the semi-major axis. In other words, the large SRP has significant impact on the high-altitude orbits, which explains the appearance of new blue regions in Fig.15 when compared with Fig.5. In addition, it is seen that the closer the orbital motion to the asteroid is, the larger the variation of e becomes. In particular, for orbits B and F, the mean value of their oscillating eccentricities increases with time and approach almost 0.12 as a result of the highly nonlinear and perturbative dynamics. For orbits C and G with relatively larger a, their oscillating eccentricities are bounded within 0.08. For orbits D and H with the largest a among all the sample orbits, their eccentricities are bounded to be less than 0.05 at the end of the integration.

Specifically, by comparing the retrograde orbit B with orbit C, orbit C has a larger a and its eccentricity reaches 0.08 at about $t=175$ when the eccentricity of orbit B reaches 0.06. There is a larger eccentricity deviation on orbit C for large SRP. All the above results show that orbit B has slightly better stability than orbit C though their semi-major axes are close to each other in Fig.5. In fact, this is the transition region where the SRP begins to dominate over the irregular gravity, which is also indicated by the more splits in the SRP direction than those in the C_{22} direction of the orbit with $a=2.2$ in Fig. 13. In addition, for both orbits D and E with the same $a=3$, the large SRP does have obvious effects on both the retrograde and the prograde motions, though the deviation is slightly larger for the prograde ones. This is probably due to the relatively better stability of the retrograde orbit to perturbations. This coincides with the conclusion that the stability of the middle- and high-altitude retrograde motion cannot be retained given the large SRP perturbation [22]. For orbit I from the yellow/stable region in Fig.15, although its eccentricity varies up to about 0.18, it is very robust to the SRP perturbation as there is almost no deviations among the green,

29

1   blue and red lines. Its eccentricity just oscillates due to the effect of the irregular

2   gravity, without the tendency of secular increase.

3   In summary, the stability of high-altitude orbits is affected by the SRP in the sense

4   that the stable region in the *a-i* plane shrinks with the increasing SRP strength,

5   especially in regions with large values of *a*. The variation of eccentricity of the

6   unstable orbit is increased by the SRP perturbation for high-altitude unstable orbits.

7   On the other hand, for the simulated unstable orbits extremely close to the asteroid,

8   the SRP perturbation is capable of preventing the eccentricity from increasing to large

9   value.

10

1
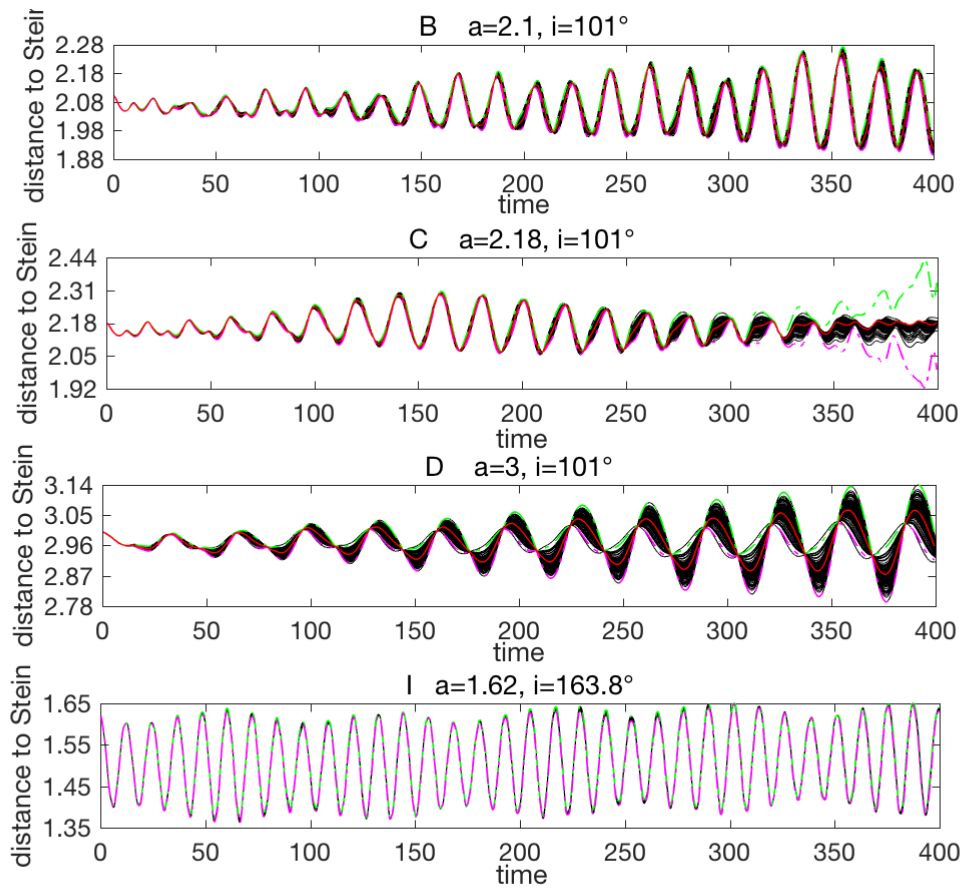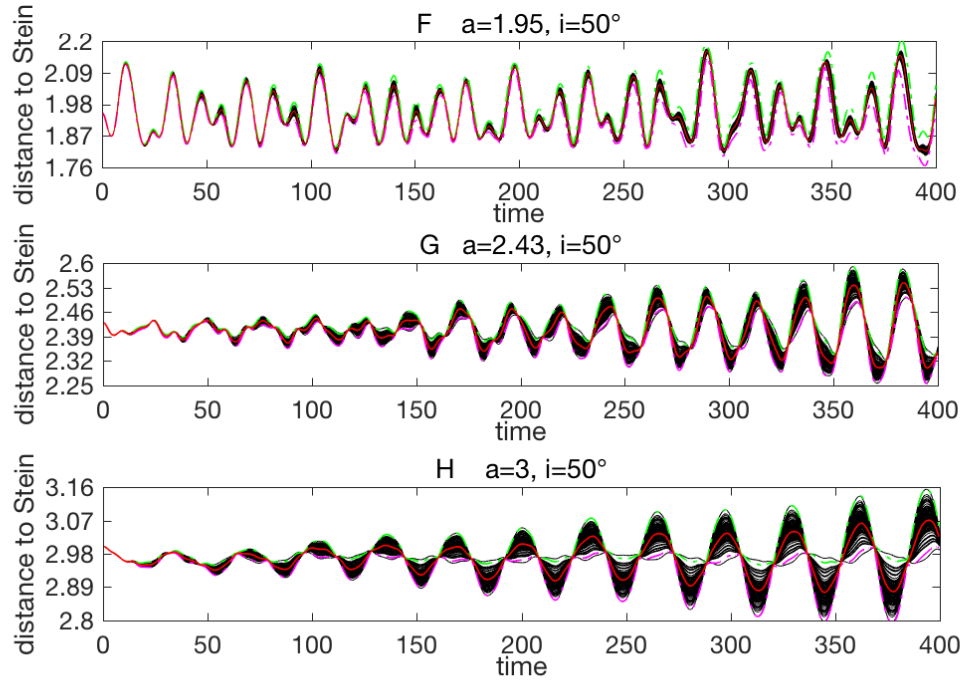
Figure 19 The distance to Stein of the center trajectory (red solid line), the MC simulations (black solid lines) and the estimated bounds (green and pink dash lines) with an integration time of t=400 including the SRP perturbation,

The bounds of the distances to Stein of these sample orbits together with the corresponding MC simulations are given in Fig.19. By comparing with the same orbit in Fig.18, it is found that the extent of the bounds or the robustness of the orbit coincides with the evolution of its orbital element e. Specifically, if the evolution of e with a large SRP deviates more from that without the SRP, e.g. orbits D and H, their bounds in Fig.19 show larger ranges than the other orbits. For orbit C, the deviation of its e for large SRP becomes large after about t=200 in Fig.18, from when the bounds of orbit C also shows similar tendency and expands significantly with time in Fig.19. For the most stable orbit I, its bounds remain extremely narrow along with time, indicating its strong robustness.

The studies above indicate that the first split time of the ADS can be used as an indicator to detect dynamical structures of the nonlinear dynamics, which are directly related to the stability, robustness and boundedness. In addition, these dynamical structures are obtained by the process of uncertainty propagation, which is different

1   from other dynamical indicators. In particular, for small body missions, the stability

2   and robustness of the motion is required if the duration of free motion arcs (i.e.

3   without maneuvers) can meet the requirements (e.g. the bounds of the state) of

4   scientific observations or the accuracy requirements for radio or laser tracking and

5   navigation [20]. The ADS can serve as a useful tool to identify this kind of motion even

6   if the uncertainties that are unavoidable in real missions are considered.

7   **4.5 The split history of the state flow with SRP**

8   Fixing the SRP perturbation at the value of 3×10^{-6}, and for the same initial orbit

9   and the same propagation time as those in Section 3.4.5, the evolutions of a and e of

10   the whole set of split trajectories are given in Fig.20. It can be seen that the first split

11   time is nearly the same as that of Fig.11, as the perturbation of the irregular gravity

12   still dominates the region close to the asteroid. Similarly, intensive splits occur at the

13   bottom-right corner, i.e. when the motion is close to the body and the effect of the

14   highly nonlinear dynamics is intensified along with time. However, there are 297

15   splits in total, which are much more than those of Fig.11 especially for $t > 85$. This

16   indicates that the SRP still plays a long-term role. It is also found that this

17   phenomenon is enhanced with the increase of the magnitude of the SRP perturbation.

18
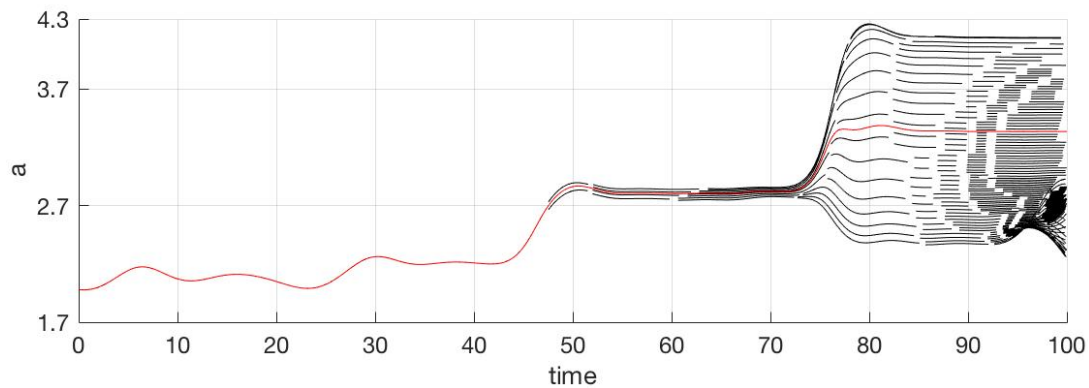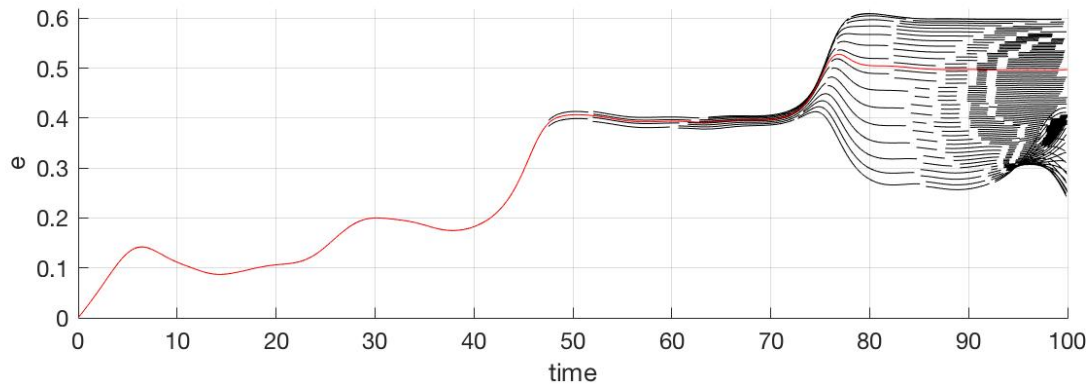
Figure 20 The evolutions of a and e for the orbit integrated with the ADS (black) and numerical integrations (red) with $a_{srp} = 3 \times 10^{-6}$.

5. Conclusions

This work contributes to exploring the idea of using ADS to detect the dynamical structure of a nonlinear dynamical system by considering model uncertainties. First, ADS is demonstrated to be capable of detecting the dynamical structure of a simple pendulum model. Taking the asteroid Stein as an example, ADS is applied to the orbital motion around a small body, considering the uncertainties from both the asteroid's gravity and the SRP.

The dynamics are found to be more sensitive to the uncertainty of the C_{22} term when compared with the C_{20} term. From the map of the first split time on the a-i plane, it is found that the motion is very sensitive to the uncertainties of the gravity field when it is close to the asteroid. Generally, the retrograde motion is relatively more stable than the prograde one, especially for low- and middle- altitude orbits when the irregular gravity dominates the dynamics. For high-altitude motion, both the retrograde and prograde motions are highly perturbed by the SRP and are significantly affected by its uncertainty. These conclusions are validated by the global contour maps of the first split time of ADS on the a-i plane and several specific examples. Also, the bounds estimated from the Taylor expansion coincide well with the MC simulations as long as the expansion meets the accuracy requirement. This fast estimation of bounds provides valuable information to select trajectories that are sufficiently robust to uncertainties.

33

For future work, the methodology presented in this paper can be extended to other potential uncertainties of the model parameters and the uncertainties of the initial state and the maneuvers.

Appendix

The normalized and non-zero coefficients of the 4th order gravity field of Stein [2]

Stein					
C_{20}	-9.78×10^{-2}	C_{33}	-3.55×10^{-4}	C_{42}	-8.55×10^{-4}
C_{22}	1.32×10^{-2}	S_{31}	1.23×10^{-3}	C_{43}	-1.79×10^{-5}
C_{30}	1.37×10^{-2}	S_{32}	-1.08×10^{-4}	S_{41}	-2.03×10^{-4}
C_{31}	1.99×10^{-3}	S_{33}	-1.04×10^{-3}	S_{42}	-1.27×10^{-4}
C_{32}	7.18×10^{-4}	C_{40}	2.52×10^{-2}	S_{43}	-7.64×10^{-6}
-	-	C_{41}	-2.96×10^{-4}	S_{44}	-1.36×10^{-5}

Acknowledgement

References

[1] D. Scheeres, Orbital Motion in Strongly Perturbed Environments, Springer, 2012.

[2] J. Melman, E. Mooij, R. Noomen, State propagation in an uncertain asteroid gravity field, Acta Astronautica, 2013, 91: 8–19.

[3] S. Hesar, D. Scheeres, J. Mcmahon, Sensitivity analysis of the OSIRIS-REx terminator orbits to maneuver errors, Journal of Guidance, Control and Dynamics, 2017, 40:1–15.

[4] J. Feng, R. Armellin, X. Hou, Orbit propagation in irregular and uncertain gravity field using differential algebra, Acta Astronautica, 2019, 161: 338-347.

[5] V. Arnold, Mathematical Methods of Classical Mechanics. Springer, 2nd edition, 1989.

[6] S. Maybeck, Stochastic Models, Estimation and Control, Academic press, New York, 1982.

[7] S. Julier, J. Uhlmann, H. Durrant-Whyte, A new approach for filtering nonlinear systems, in: Proceedings of IEEE American Control Conference, 1995, 1628–1632.

[8] G. Terejanu, P. Singla, T. Singh, P.D. Scott, Uncertainty propagation for nonlinear dynamic systems using gaussian mixture models, Journal of Guidance, Control and Dynamics, 2008, 31(6): 1623–1633.

[9] N. Wiener, The homogeneous chaos, Am. J. Math. 1938, 60(4): 897–936.

[10] M. Vasile, C. Absil, A. Riccardi, Set propagation in dynamical systems with generalised polynomial algebra and its computational complexity, Commun Nonlinear Sci Numer Simulat, 2019, 75: 22–49.

[11] M. Berz, Modern Map Methods in Particle Beam Physics, Academic Press, New York, 1999: 82–96.

[12] R. Armellin, P. Di Lizia, F. Bernelli-Zazzera, M. Berz, Asteroid close encounters characterization using differential algebra: the case of Apophis, Celest. Mech. Dyn. Astron., 2010, 107(4): 451-470.

[13] R. Armellin, P. Di Lizia, F. Bernelli-Zazzera, A high order method for orbital conjunctions analysis: sensitivity to initial uncertainties, Advances in Space Research, 2014, 53(3): 490–508.

[14] A. Wittig, P. Di Lizia, F. Bernelli-Zazzera, R. Armellin, K. Makino, M. Berz, Propagation of large uncertainty sets in orbital dynamics by automatic domain splitting, Celestial Mechanics and Dynamical Astronomy, 2015, 122(3): 239-261.

[15] Cl. Froeschle, The Lyapunov characteristic exponents-applications to celestial mechanics. Celestial Mechanics, 1984, 34: 95–115.

[16] Haller, G. Distinguished material surfaces and coherent structures in three-dimensional fluid flows. Physica D, 2001, 149: 248-277.

[17] D. Perez-Palau, J. Masdemont, G. Gomez, Tools to detect structures in dynamical systems using Jet Transport. Celestial Mechanics and Dynamical Astronomy, 2015, 123: 239–262.

1   [18] P. Panicucci, B. Bercovici, E. Zenou, et al., Uncertainties in the gravity spherical

2   harmonics coefficients arising from a stochastic polyhedral shape. Celestial

3   Mechanics and Dynamical Astronomy, 2020, 132, 23.

4   [19] S. Kent, "Lagrangian coherent structures: Generalizing stable and unstable

5   manifolds to non-autonomous dynamical systems," Tucson, AZ, 2008.

6   [20] H. Hussmann, J. Oberst, K. Wickhusen, et. al, Stability and evolution of orbits

7   around the binary asteroid 175706 (1996 FG3): Implications for the MarcoPolo-R

8   mission, Planetary and Space Science, 2012, 70(1): 102-113.

9   [21] Moore R, Kearfott R, Cloud M, Introduction to Interval Analysis. Cambridge

10   University Press, 2009.

11   [22] J. Feng, X. Hou, Secular dynamics around small bodies with solar radiation

12   pressure, Communications in Nonlinear Science and Numerical Simulation, 2019, 76:

13   71-91.